Chapter V

Phase Separation in Wurtzite $CuIn_xGa_{1-x}S_2$ NPs

V.1 Introduction

The synthesis of wurtzite CIS nanoparticles was first reported by Pan *et al.* in 2008 [44]. Since then, numerous reports on wz-CIS were published [47, 178, 190, 195, 224]; however, there are only a few researchers reported the synthesis of wz-$CuIn_xGa_{1-x}S_2$ (CIGS) NPs [182, 197, 224]. With increasing concentration of Ga, the optical and electrical properties of wz-CIGS are modified. The bandgap of the $CuIn_xGa_{1-x}S_2$ nanocrystals increases from 1.53 eV for CIS to 2.48 eV for CGS with a variation of x from 0 to 1 [224]. The reported value of carrier mobility of wz-CIGS is about 4.85 cm^2/Vs [197], which is greater than the wz-CIS (0.5cm^2/Vs) [225].

The synthesis process for the wz-CIGS NPs are generally similar to wz-CIS with the addition of an appropriate precursor for incorporation of gallium. From the HSAB theory, indium insertion into the nanocrystal lattice prior to gallium is expected as Ga^{3+} is a harder acid compared to In^{3+} [182]. Gallium incorporation generally occurs at slightly higher temperature. There are few studies on the effect of temperature, composition variation and ligand on the morphology of quaternary copper chalcogenides [182, 197, 224]. The detailed analysis of addition of a series of amine ligands of differing alkyl chain length on the morphology was discussed

by Coughlan *et al.* [182]. Recently, the synthesis of wz-$CuIn_xGa_{1-x}Se_2$ nanocrystals was reported in order to avoid the selenization process [226, 227]. Houck *et al.* [226] discussed rate of nucleation and growth of $CuInSe_2$ on Ga incorporation and its effect on the morphology.

It is established that gallium incorporation results in structural distortion, non-homogeneous shape, and distribution of particles [182]. However, the effect of Ga substitution on particle morphology and structure has not been explored much. In this chapter, we synthesize the metastable $CuIn_xGa_{1-x}S_2$ (x = 1, 0.7, 0.5, 0.3, and 0) NPs with the use of a mixture of strongly coordinating solvents (OAm) and the metal precursor of acetylacetonate sources and have done an in-depth structural analysis using X-ray diffraction (XRD) and transmission electron microscopy (TEM) to demonstrate the evolution of structure and morphological change on the substitution of gallium in $CuIn_xGa_{1-x}S_2$ (x= 0-1).

V.2 A Review of Relevant Literature

The first report of wz-CIGS with varying In/Ga ratio was published by Wang *et al.* [224]. It was pointed out for CIS that the presence of coordinating agent (oleylamine) promotes homogeneous distribution of rod-shaped particles which becomes non-homogeneous in shape on partial substitution of Ga for In. It was reported that the variation in morphology of NPs with varying Ga/In ratios was probably caused by differences in the binding strength of the respective cations with TOPO, OAm and ODE [224, 228]. On the similar line, Coughlan *et al.* [182] reported the change in morphology and structure on gallium incorporation as a function of time and temperature. They also showed a change in aspect Ratio (L/D),

L=length, D=diameter; on utilizing the amine ligands with different alkyl chain length. Connor *et al.* [229] and Gusain *et al.* [230] reported solution processing of wz-CIGS with limited discussion on the morphology and structural relation. Similarly, Zhang *et al.* [197] discussed the effect of solvent on the electrical and optical properties of wz-CIGS. We have found that the reports claiming the formation of pure wz-CIGS lacks in-depth analysis. In a few reports, clear shoulders in the XRD peaks of partial Ga substituted powders were observed ($CuIn_{0.75}Ga_{0.25}S_2$) which were attributed to the lattice distortion [224, 230]. Shoulder formation and observation of more than one morphology could also be due to phase separation; however, no such investigation has ever been published to the best of our knowledge. Although the earlier reports have established the formation mechanism of wz-$CuIn_xGa_{1-x}Se_2$ [182, 224, 231] to a large extent, the analysis of structure, chemistry, morphology correlation needs to be established.

V.3 Experimental Procedure

The synthesis of $CuInS_2$ NPs by solution processing route using Cu(acac), In(acac) as metal salts and OAm and TOPO as solvents were described in chapter IV. In this chapter $CuIn_xGa_{1-x}S_2$ wurtzite NPs, with x varying from 1 to 0, were synthesized. Quaternary compounds such as $CuIn_{0.7}Ga_{0.3}S_2$, $CuIn_{0.5}Ga_{0.5}S_2$, $CuIn_{0.3}Ga_{0.7}S_2$ and $CuGaS_2$, have been made by replacing an appropriate amount of In(acac) with Ga(acac).

V.4 Results and Discussion

XRD analysis revealed that the nanocrystals are composed of wz-CIS/CIGS/CGS with no evidence of crystalline binary sulfide impurities such as Cu_2S or In_2S_3

(Figure V.1(a)). The XRD patterns were compared with earlier published crystal structure data for wz-CIS [44, 178, 190, 232, 233]. The diffraction peaks located at 2θ values 26.36, 27.75, 29.80, 38.62, 46.40, 50.37, 54.16, 54.97, 56.18, 57.33, 61.95, and 64.15 were assigned to the $(10\bar{1}0)$, (0002), $(10\bar{1}1)$, $(10\bar{1}2)$, $(11\bar{2}0)$, $(10\bar{1}3)$, $(11\bar{2}2)$, $(20\bar{2}0)$, $(20\bar{2}1)$, (0004), $(20\bar{2}2)$, and $(10\bar{1}4)$ crystallographic planes of the wurtzite phase, respectively. On partial substitution of Ga for In (x = 0.7, 0.5, 0.3) in wz-CIS, the XRD pattern showed a systematic peak shift toward a higher angle **(Figure V.1(b))**. This systematic peak shift was due to smaller Ga^{3+} ions replacing In^{3+}, which resulted in a reduction in the lattice parameter. In addition, the intensity of XRD peaks also varied on substituting Ga for In atom due to the change in the scattering factor.

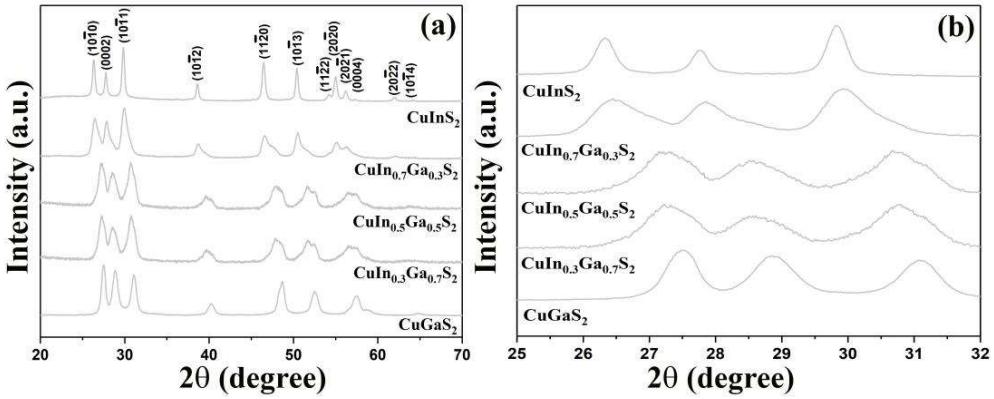

Figure V.1 (a) X-ray diffraction of $CuIn_xGa_{1-x}Se_2$ as synthesized wurtzite NPs with varying x, (b) Magnification image of the (0002), $(11\bar{2}0)$, and $(10\bar{1}3)$ peaks show a clear shift toward a higher angle.

The crystallite size ~36.6 nm for the CIS was estimated from the XRD peak broadening. With the gallium substitution, the XRD peak broadening increased. According to Kruszynska *et al.* [196], relative intensities vary because of changes

in shape and texture. On partial substitution of Ga for In (x = 0.7, 0.5, 0.3), the XRD peaks not only shifted to a higher angle but shoulders appeared on the XRD peaks. These observations had also been made by earlier researchers, which were attributed to the lattice distortion due to Ga substitution [224]. However, the systematic appearance of the shoulder toward a higher 2θ is also possible due to the presence of a closely related more than one phase. This possibility was never examined in the earlier reports [224, 230].

In this case, all the XRD peaks could be deconvoluted using OriginPro 2017(64-bit) software into two or three peaks: two peaks for the composition $CuIn_{0.7}Ga_{0.3}S_2$ and three peaks for $CuIn_{0.5}Ga_{0.5}S_2$ and $CuIn_{0.3}Ga_{0.7}S_2$ with slightly different 2θ values. The deconvoluted XRD peaks corresponding to (0002), $(11\bar{2}0)$, and $(10\bar{1}3)$ planes for each composition are depicted in **Figure V.2**. Each set of peaks obtained as a result of deconvolution could be indexed independently to different wurtzite phases with varying lattice parameters. As a result of deconvolution, two sets of diffraction planes could be obtained for $CuIn_{0.7}Ga_{0.3}S_2$ composition **(Figure V.2(a–c))** and two sets of corresponding lattice parameters were calculated **(Table V.1)**. Both the XRD patterns could be indexed independently to wurtzite phases. On the other hand, the XRD patterns obtained from $CuIn_{0.5}Ga_{0.5}S_2$ and $CuIn_{0.3}Ga_{0.7}S_2$ could be deconvoluted into three wurtzite phases and with varying lattice parameters listed in **Table V.1**.

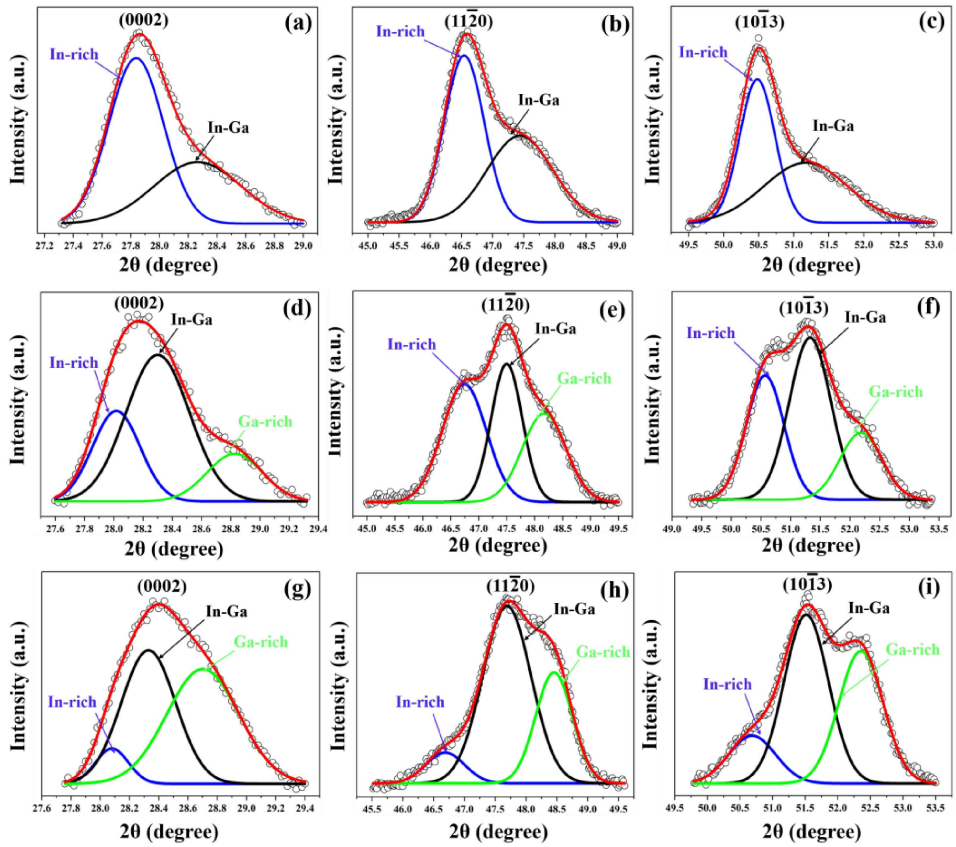

Figure V.2 Deconvolution of XRD peaks corresponding to (0002), (11$\bar{2}$0), and (10$\bar{1}$3) planes for $CuIn_{0.7}Ga_{0.3}S_2$ (a–c), $CuIn_{0.5}Ga_{0.5}S_2$ (d, e), and $CuIn_{0.3}Ga_{0.7}S_2$ (g–i).

Table V.1 Lattice parameters of CIS, CGS and phase separated compositions.

Lattice parameter (Å) calculation by Nelson-Riley function[234]					
CIS		**CIGS**			**CGS**
		In-rich	**In-Ga**	**Ga-rich**	
***a*=*b*=3.91 ± 0.01** ***c*= 6.43 ± 0.01**	$CuIn_{0.7}Ga_{0.3}S_2$	*a*=*b*=3.89 *c*= 6.41	*a*=*b*=3.82 *c*=6.31	-	*a*=3.74 ± 0.04 *c*= 6.20 ± 0.02
	$CuIn_{0.5}Ga_{0.5}S_2$	*a*=*b* =3.88 *c*= 6.37	*a*=*b*=3.83 *c*= 6.31	*a*=*b* =3.78 *c*=6.21	
	$CuIn_{0.3}Ga_{0.7}S_2$	*a*=*b* =3.89 c= 6.36	*a*=*b* =3.81 *c*= 6.30	*a*=*b* =3.76 *c*=6.22	

It was suspected that there could be the formation of more than one wurtzite phases with varying compositions. The two sets of lattice constant (*a*) calculated from the deconvoluted XRD peaks of $CuIn_{0.7}Ga_{0.3}S_2$ sample were 3.89 A˚ for phase I and 3.82 A˚ for phase II. The lattice parameter '*a*' of the phase I was very close to *a* = *b* = 3.91 A˚ earlier obtained for the phase pure CIS, while the lattice parameter of phase II was somewhere in between that of the CIS and CGS [192, 224]. Since CIGS is a solid solution of CIS and CGS, assuming it follows Vegard's law, a calibration curve was plotted for the lattice parameter as a function of Ga substitution from earlier reports **(Figure V.3)** [181, 224].

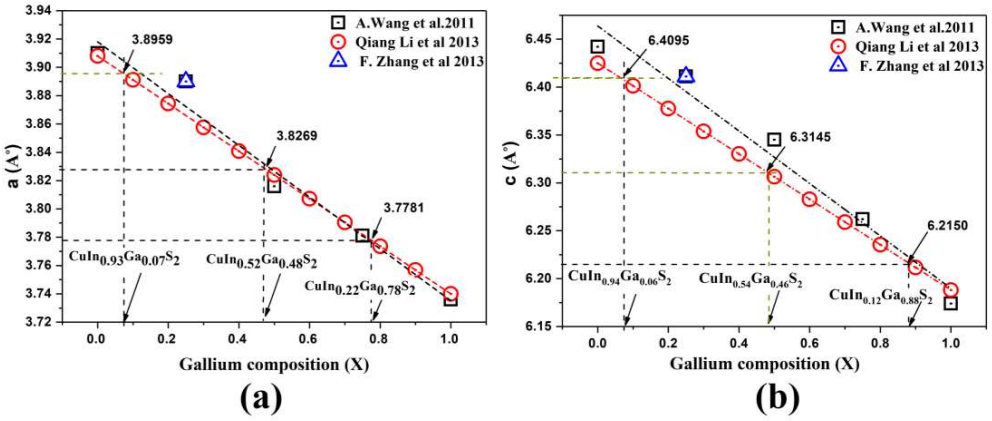

Figure V.3 Calculation of composition for In-rich, In-Ga(1:1) and Ga- rich using lattice constant *a*=*b* (a) and *c* (b) by implying Vegard's law.

The compositions of the phases I and II (estimated to from the calibration curve) were $CuIn_{0.93}Ga_{0.07}S_2$ (In-rich phase) and $CuIn_{0.52}Ga_{0.48}S_2$ (In–Ga phase), respectively. Similar compositions were obtained from the lattice parameter c. The composition obtained separately from both the lattice parameters '*a*' and '*c*' was close and is tabulated in **Table V.2**. When the Ga substitution was increased, as in

the case of $CuIn_{0.5}Ga_{0.5}S_2$ and $CuIn_{0.3}Ga_{0.7}S_2$, the XRD pattern could be deconvoluted into three wurtzite phases with three different compositions: In-rich, In–Ga, and an additional Ga-rich phase. For the $CuIn_{0.5}Ga_{0.5}S_2$ sample, three lattice parameters (*a*) were estimated to be 3.88, 3.83, and 3.78 A˚ corresponding to In-rich, In–Ga, and Ga-rich phase as listed in **Table V.2.**

Table V.2 Composition analysis of In-rich, In–Ga, and Ga-rich of wz-CIGS.

		CIGS		
	Ga	**0.3**	**0.5**	**0.7**
In-rich	Lattice parameter (Å)	a=b=3.89	a=b=3.88	a=b=3.89
	Composition	$CuIn_{0.93}Ga_{0.07}S_2$	$CuIn_{0.88}Ga_{0.12}S_2$	$CuIn_{0.91}Ga_{0.09}S_2$
	Lattice parameter (Å)	c=6.41	c=6.37	c=6.36
	Composition	$CuIn_{0.94}Ga_{0.06}S_2$	$CuIn_{0.78}Ga_{0.22}S_2$	$CuIn_{0.76}Ga_{0.24}S_2$
In-Ga	Lattice parameter (Å)	a=b=3.82	a=b=3.83	a=b=3.81
	Composition	$CuIn_{0.52}Ga_{0.48}S_2$	$CuIn_{0.47}Ga_{0.53}S_2$	$CuIn_{0.44}Ga_{0.56}S_2$
	Lattice parameter (Å)	C=6.31	c=6.31	c=6.30
	Composition	$CuIn_{0.54}Ga_{0.46}S_2$	$CuIn_{0.48}Ga_{0.52}S_2$	$CuIn_{0.47}Ga_{0.53}S_2$
Ga-rich	Lattice parameter (Å)		a=b=3.78	a=b=3.76
	Composition		$CuIn_{0.22}Ga_{0.78}S_2$	$CuIn_{0.13}Ga_{0.87}S_2$
	Lattice parameter (Å)		c=6.21	c=6.22
	Composition		$CuIn_{0.12}Ga_{0.88}S_2$	$CuIn_{0.15}Ga_{0.85}S_2$

Similarly, in the case of $CuIn_{0.3}Ga_{0.7}S_2$, the three obtained lattice parameters (*a*) 3.89, 3.81, and 3.76 A˚ were close to that obtained in the case of $CuIn_{0.5}Ga_{0.5}S_2$ samples and could again be assigned to the In-rich, In–Ga, and Ga-rich phases. The abundance of the deconvoluted phases was estimated from the integrated intensities using the structure factor (F), multiplicity factor (p), and Lorentz polarization factor. Theoretical relative intensities of the In-rich, In–Ga, and Ga-rich phases with varying Ga substitutions are depicted in **Figure V.4**.

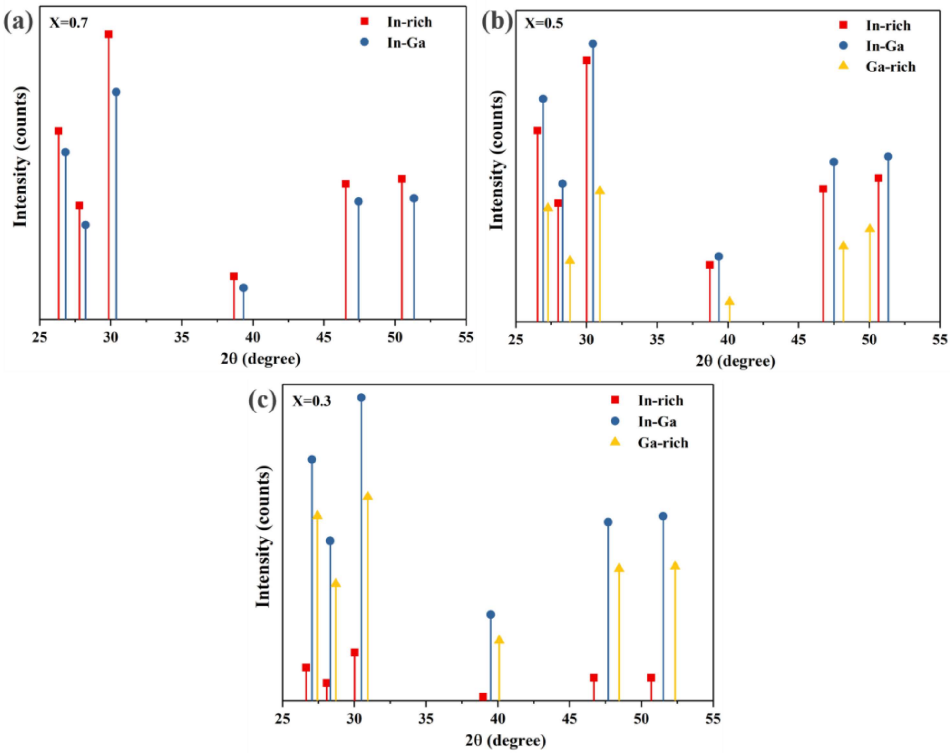

Figure V.4 Theoretical relative intensities of the XRD peaks of (a) X=0.7, (b) X=0.5, and (c) X=0.3 were calculated using structure factor (F), multiplicity(p), polarization and Lorentz factor assuming the absorption and temperature factor for both phases being equal for In-rich and In.

The phase fraction of In-rich and Ga–In phases in the $CuIn_{0.7}Ga_{0.3}S_2$ was estimated to be 0.57 and 0.43 respectively. An additional Ga-rich phase was observed in the case of $CuIn_{0.5}Ga_{0.5}S_2$ and $CuIn_{0.3}Ga_{0.7}S_2$. The phase fraction of the Ga-rich phase increased from almost zero to 0.27 and 0.45, while at the same time, the fraction of In-rich phase reduced from almost 0.57 to 0.31 and 0.08 when Ga substitution is increased from 0.3 to 0.5 and 0.7, respectively. The In–Ga phase increased marginally from 0.43 to about 0.47, with Ga substitution increasing from 0.3 to 0.7. The change in phase fractions of In-rich, In–Ga, and Ga-rich phases is depicted in **Figure V.5**.

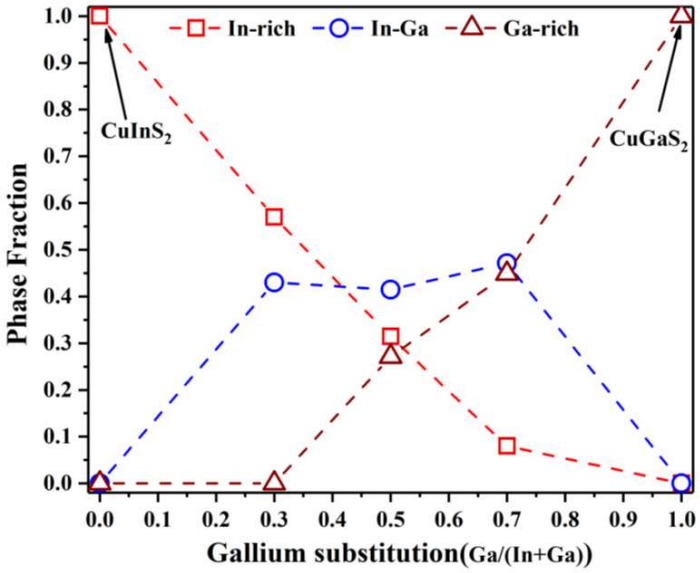

Figure V.5 Phase fraction of In-rich, In–Ga, and Ga-rich phase as a function of Ga Substitution.

The morphology, composition, and structure correlation of the synthesized wurtzite NPs were analysed in TEM. The bright-field image of wz-CIS NPs had a uniform particulate shape with an oval morphology (narrow ends and quasi-round bodies)

having a mean diameter and length of 23 ± 1.6 and 39 ± 2.6 nm, respectively **(Figure V.6(a))**. These values obtained from TEM images are in good agreement with the crystallite size ~36 nm as calculated from the powder X-ray diffraction patterns **(Figure V.1(a))** using the Scherrer equation. Kruszynska *et al.* [196] and Lu *et al.* [181] reported nearly similar nanostructure morphology using acetate and nitrate as metal precursors respectively.

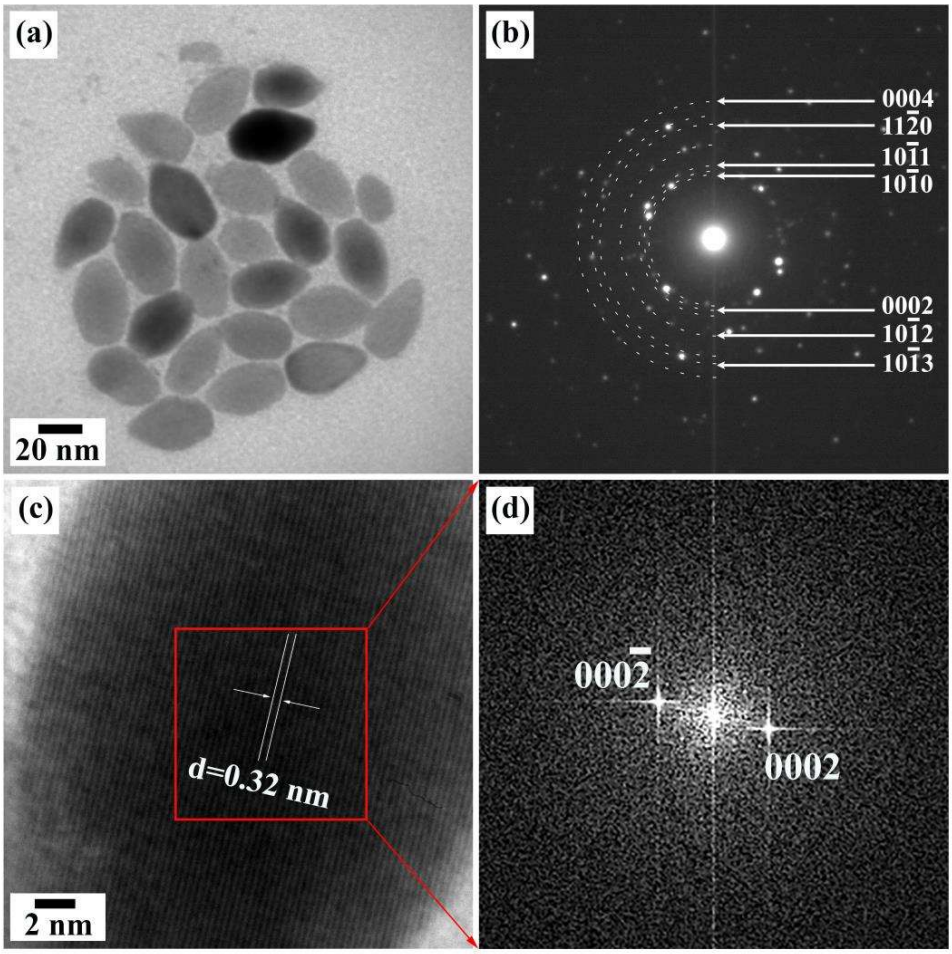

Figure V.6 (a) Bright field TEM image, (b) SAED pattern of CIS nanocrystals, (c) HRTEM image of a CIS NPs shows a lattice inter-planar spacing of 0.32 nm, (d) fast Fourier transform (FFT) patterns are calculated from the HRTEM image.

Each ring of the selected area electron diffraction (SAED) pattern was accounted for wz-CIS and was indexed to $(10\bar{1}0)$, (0002), $(10\bar{1}1)$, $(10\bar{1}2)$, $(11\bar{2}0)$, $(10\bar{1}3)$, and (0004) crystallographic planes **(Figure V.6(b))**. High resolution TEM (HRTEM) images revealed that the NPs were single crystalline, and the d-spacing of the lattice fringes (0.32 ± 0.01 nm) was close to that of the plane (0002) of the wz-CIS structure **(Figure V.6(c))**.

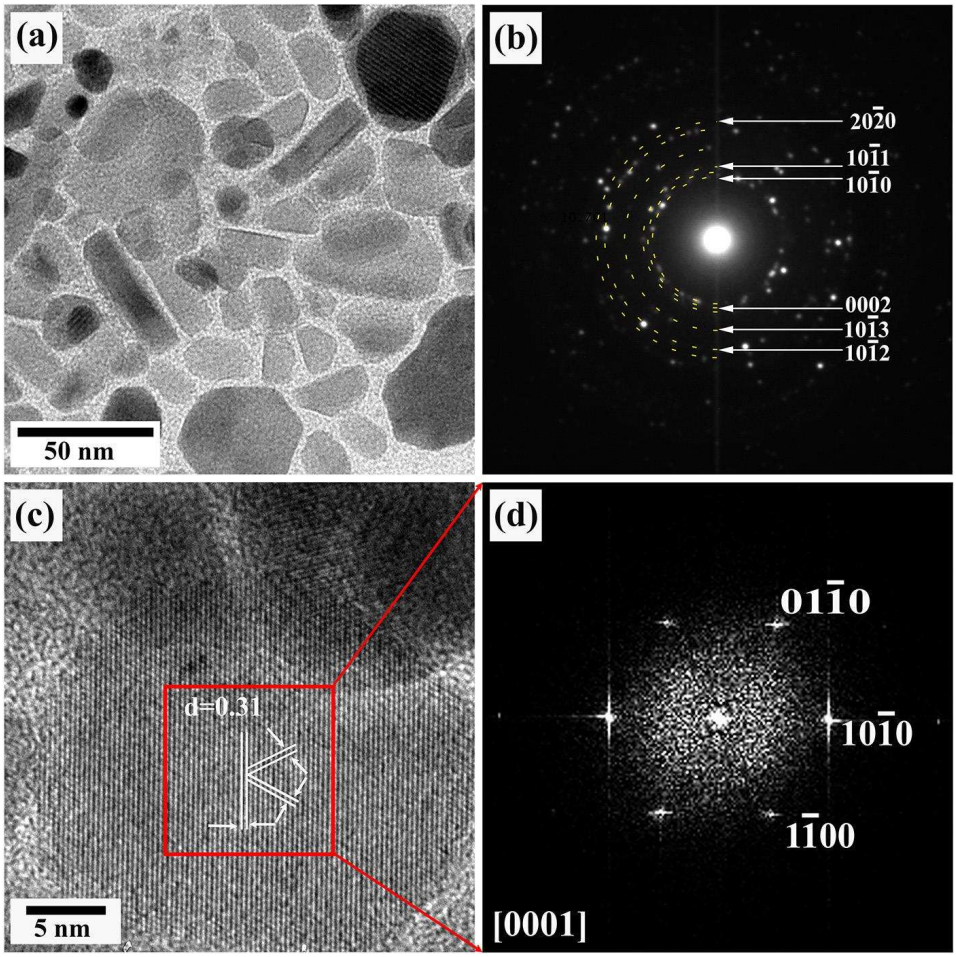

Figure V.7 (a) Bright field TEM image, (b) SAED pattern of CGS nanocrystals, (c) HRTEM image of CGS nanoparticles shows a lattice inter-planar spacing of 0.31 nm, (d) FFT patterns calculated from the HRTEM image.

In contrast to CIS and CGS, where more or less uniform morphology was observed, more than one particle morphologies could be observed in the case of $CuIn_xGa_{1-x}S_2$ sample, which varied with the Ga substitution. In the case of $CuIn_{0.7}Ga_{0.3}S_2$, two different particle morphologies: hexagonal/equiaxed and rod-like, could be observed. A representative TEM bright-field image showing different morphologies is depicted in **Figure V.8(a)**. As-synthesized $CuIn_{0.7}Ga_{0.3}S_2$ nanocrystals were slightly irregularly faceted particles with predominantly rod-like and hexagonal morphology (marked as letters B and A, respectively). From XRD, it was established that the $CuIn_{0.7}Ga_{0.3}S_2$ NPs had two phases: In-rich and In– Ga. It was suspected that the two morphologies belonged to these two phases. The average length of the rod-like particles and the size of hexagonal particles were 24 ± 7.9 and 14 ± 2.3 nm, respectively, which was close to the crystallite sizes, about 17 and 10 nm as calculated from the XRD pattern using the Scherrer equation. It has been widely accepted that during the synthesis of $CuIn_xGa_{1-x}S_2$ nanocrystals, nucleation of Cu–S takes place, which is preceded by the In incorporation [21, 38, 41]. This happens at a reaction temperature close to 210 ^oC. As a result of CIS formation, the remaining solution becomes richer in Ga, and as a result, a phase relatively richer in Ga (an In–Ga phase in this case) forms at later stages. It has also been reported that the presence of amines alters the morphology [182]. In this case, the solution gets depleted of amines at later stages, and therefore, the phases richer in Ga, which nucleates at the later stages, develop a distinct morphology. This leads to the evolution of predominately different morphologies with varying Ga content. SAED obtained from both morphologies had clear diffraction rings, which could be indexed to the wurtzite phase. Clear lattice fringes with the interplanar spacing of 0.33 and 0.29 nm could be observed in HRTEM images of rod-like particles

(Figure V.8(b)) and hexagonal particles **(Figure V.8(c))** corresponding to $(10\bar{1}0)$ and $(10\bar{1}1)$ planes, respectively.

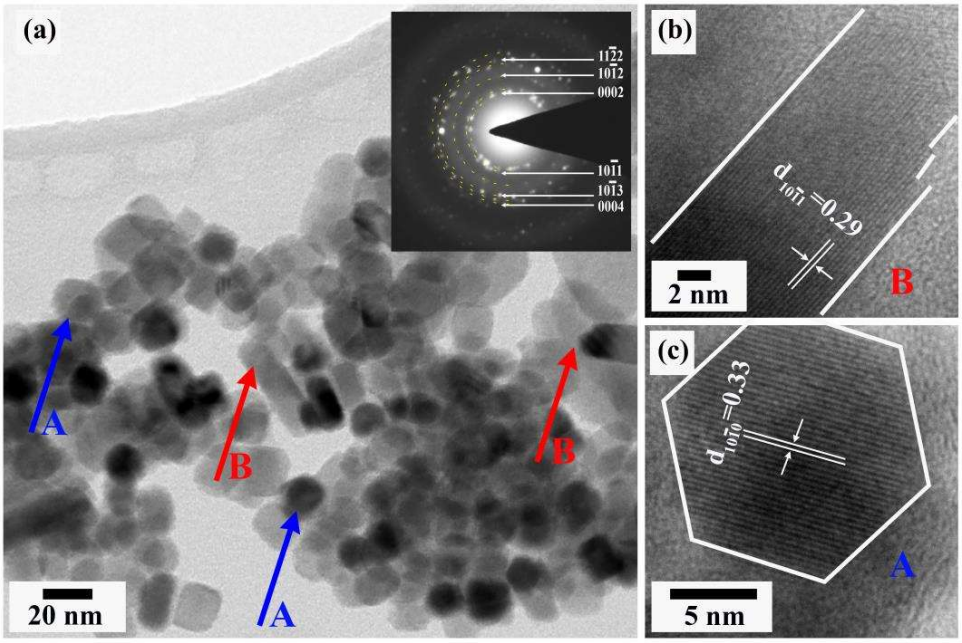

Figure V.8 (a) Bright field TEM image inserted SAED pattern of CIGS NPs, (b) HRTEM image of an In-rich nanoparticle shows a lattice inter-planar spacing of 0.33 nm, (c) HRTEM image of an In–Ga nanoparticle shows a lattice inter-planar spacing of 0.29 nm.

On increasing substitution of gallium (i.e., x = 0.5, 0.3), three different particle morphologies: rod-like, hexagonal/equiaxed, and tadpole, could be observed in the case of $CuIn_{0.5}Ga_{0.5}S_2$ and $CuIn_{0.3}Ga_{0.7}S_2$ NPs. A representative TEM bright-field image showing different morphologies is depicted in **Figure V.9(a)** for $CuIn_{0.5}Ga_{0.5}S_2$. As-synthesized $CuIn_{0.5}Ga_{0.5}S_2$ NPs were slightly irregularly faceted particles with either hexagonal morphology, rod-like, or tadpole (marked as letters A, B, and C, respectively, in **Figure V.9(a)**). From XRD, it was established that the

$CuIn_{0.5}Ga_{0.5}S_2$ and $CuIn_{0.3}Ga_{0.7}S_2$ NPs had three phases: In-rich, In–Ga, and Ga-rich. From the TEM analysis of $CuIn_{0.7}Ga_{0.3}S_2$, it is established that In-rich phase had rod-like morphology, while the In–Ga phase was hexagonal or equiaxed. Therefore, the tadpole-like morphology must be the Ga-rich phase. The average length of the rod-like particles and the size of hexagonal particles were 48 ± 11.2 and 20 ± 3.2 nm, respectively.

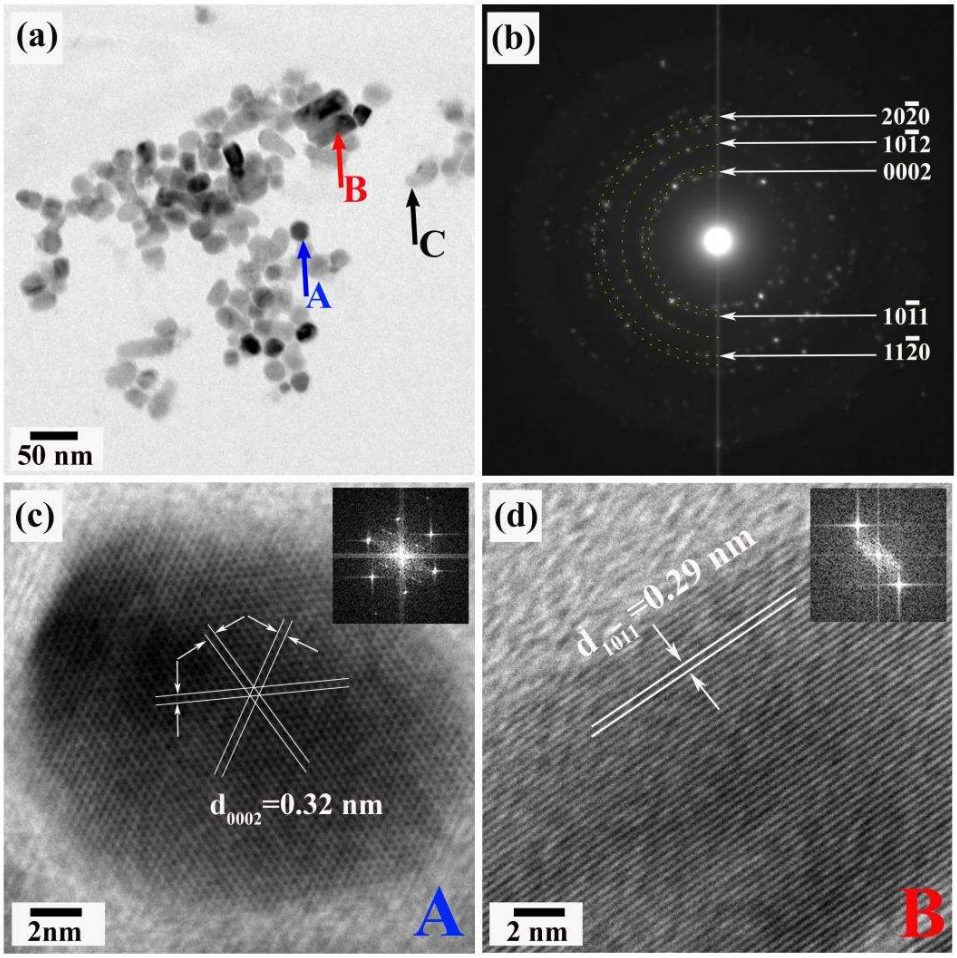

Figure V.9 (a) Bright field TEM image, (b) SAED pattern of CIGS nanocrystals of $CuIn_{0.5}Ga_{0.5}S_2$ NPs, (c) HRTEM image of a hexagonal/equiaxed shows a lattice inter-planar spacing of 0.32 nm, (d) HRTEM image of a rod-like nanoparticle shows a lattice inter-planar spacing of 0.29 nm.

When x = 0.5, each ring of the SAED pattern was accounted for $CuIn_{0.5}Ga_{0.5}S_2$ and was indexed to (0002), (10$\bar{1}$1), (10$\bar{1}$2), (11$\bar{2}$0), and (20$\bar{2}$0) crystallographic planes **(Figure V.9(b))**. High-resolution TEM images revealed that the NPs were single crystalline, and the d-spacing of the lattice fringes 0.32 and 0.29 nm **(Figure V.9(c) and (d))** were close to that of the d-spacing of (0002) and (10$\bar{1}$1) planes of the wz-CIS structure.

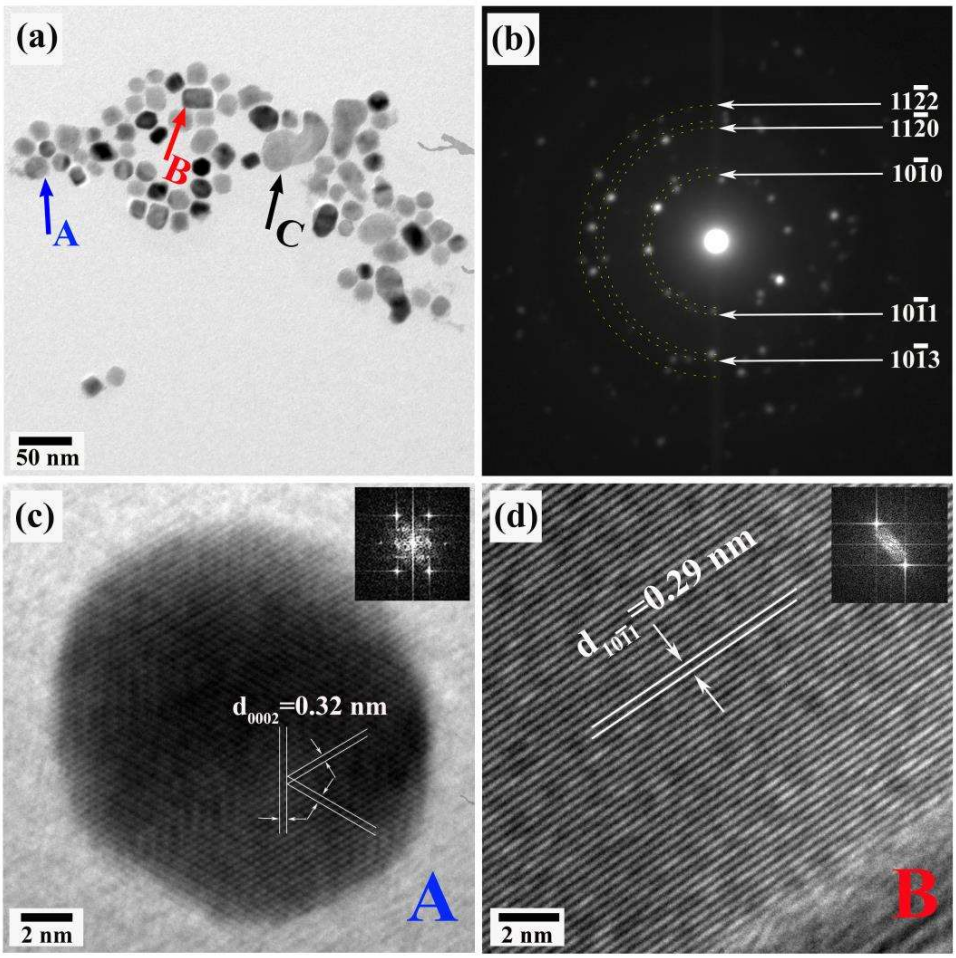

Figure V.10 (a) Bright field TEM image, (b) SAED pattern of CGS nanocrystals of $CuIn_{0.3}Ga_{0.7}S_2$ NPs, (c) HRTEM image of a hexagonal/equiaxed shows a lattice inter-planar spacing of 0.32 nm, (d) HRTEM image of a rod-like nanoparticle shows a lattice inter-planar spacing of 0.29 nm.

In comparison with $CuIn_{0.5}Ga_{0.5}S_2$, the hexagonal morphology was more predominant in the case of $CuIn_{0.3}Ga_{0.7}S_2$ NPs, as shown in **Figure V.10(a)**. The edge of the hexagonal particles was 19 ± 1.8 nm, which matched with the crystallite size of ~16 nm as estimated from XRD peak broadening using the Scherrer equation. The presence of greater amounts of hexagonal particles, when compared to the rod-like and tadpole morphology, was in line with the estimation of larger fraction of In–Ga phase (0.47) with the greater Ga substitution when compared with the abundance of rod-like and tadpole. This further confirmed that hexagonal/polygonal morphology belonged to Ga–In phase. A representative TEM bright-field image showing different morphologies for $CuIn_{0.3}Ga_{0.7}S_2$ is depicted in **Figure V.10(a)**. Each ring of the SAED pattern was accounted and was indexed to $(10\bar{1}0)$, $(10\bar{1}1)$, $(11\bar{2}0)$, $(10\bar{1}3)$, and $(11\bar{2}2)$ crystallographic planes **(Figure V.10(b))**. HRTEM images showed that the NPs were single crystalline, and the d-spacing of the lattice fringes 0.32 and 0.29 nm were close to that of the plane (0002) and $(10\bar{1}1)$ of the wurtzite structure **(Figure V.10(c) and (d))**.

In order to further check the composition of the different morphologies, chemical analysis of individual particles was performed in scanning transmission electron microscopy (STEM) mode for $CuIn_{0.7}Ga_{0.3}S_2$. Bright field TEM of a rod-like nanoparticle is shown in **Figure V.11(a)**, while its corresponding SAED pattern is indexed along zone axis $(5\bar{1}\bar{4}3)$ in **Figure V.11(b)**. High-angle annular dark-field (HAADF) image of a rod-like nanoparticle **(Figure V.11(c))** was featureless and was uniformly bright thought the particle indicating a uniform chemical composition. EDS mapping of the randomly selected rod-like nanoparticle **(Figure V.11(d–g))** illustrates that all the elements Cu, In, Ga, and S were homogeneously

distributed along the rod with In being present in much greater concentrations **(Figure V.11(e))** when compared to Ga **(Figure V.11(f))**. STEM-EDS results showed that rod-like nanoparticle was richer in indium, which was in good agreement with the XRD results.

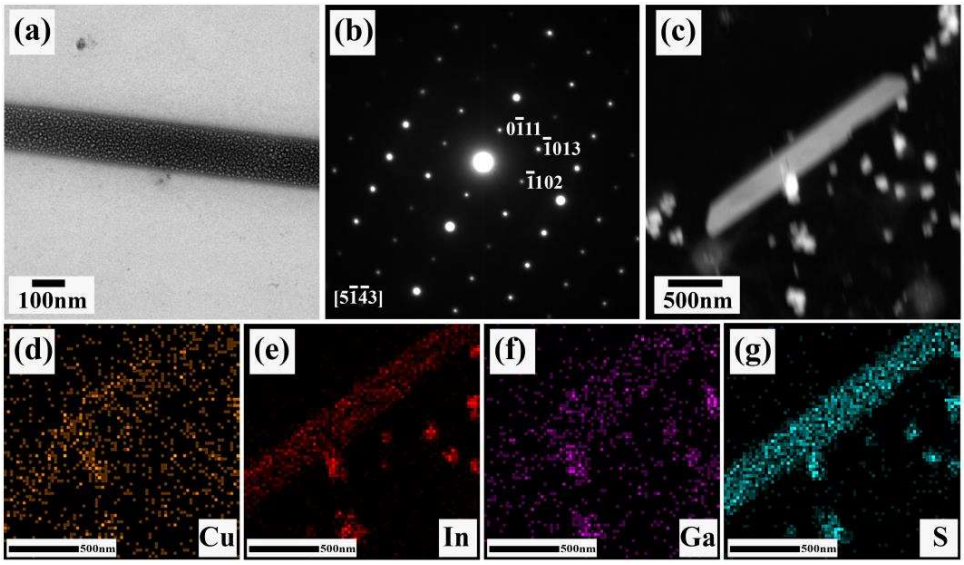

Figure V.11 (a) Bright field TEM image, (b) SAED pattern, and (c) HAADF-STEM image of indium-rich composition, (d–g) STEM-EDS mapping of rod-shape nanoparticle.

Figure V.12(a) and (b) depicts the bright field TEM image of a randomly selected hexagonal NP and its corresponding SAED pattern, which could be indexed along [0001] zone axis. HAADF-STEM image of the irregular hexagon-shaped NP was uniformly bright, indicating the chemical homogeneity. EDS mapping of the arbitrarily chosen NP is illustrated in **Figure V.12(d–g)**. While all the elements were distributed homogeneously over the NP, the intensity of Ga **(Figure V.12(f))** was much greater when compared to that of the In. This was in contrast to the observation made for the rod-like NP. This denoted that while the rod-like particle

was rich in In and the hexagonal particles were comparatively richer in Ga. The STEM-EDS result clearly established our assertion that the $CuIn_{0.7}Ga_{0.3}S_2$ NPs indeed phase-separated into two distinct chemical compositions; In-rich and In–Ga (relatively richer in Ga), both having wurtzite structure formed at different stages of processing resulting in two distinct morphologies: rod-like and irregular hexagon in this case.

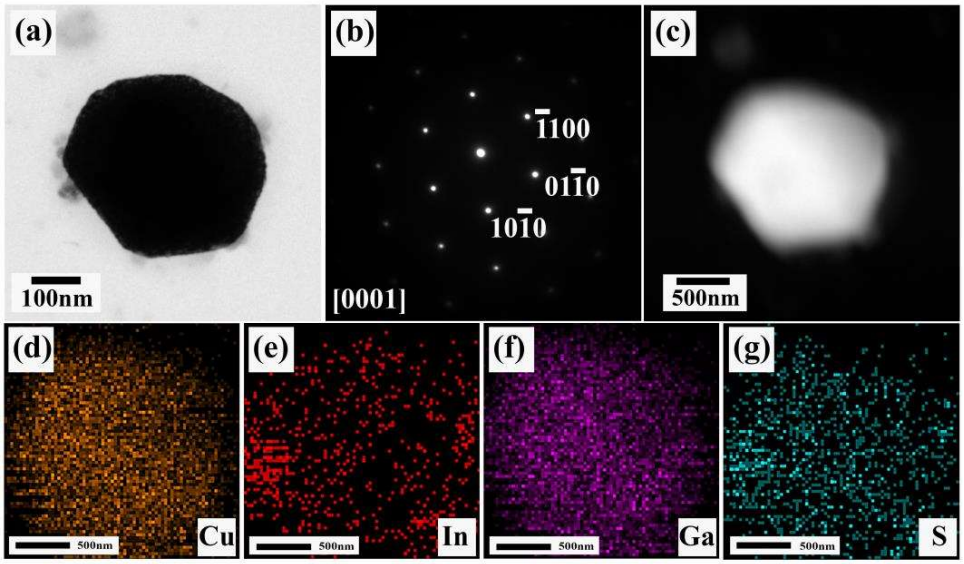

Figure V.12 (a) Bright field TEM image, (b) SAED pattern, (c) HAADF-STEM image of gallium-rich composition, (d–g) STEM-EDS mapping of hexagon-shape NP

Figure V.13 shows UV–VIS absorption spectra and Tauc plots for the as-synthesized wz-$CuIn_xGa_{1-x}S_2$ NPs measured at room temperature. The absorption spectra of the $CuIn_xGa_{1-x}S_2$ NPs showed a blue shift with increasing Ga content [27, 224]. The absorption spectra of all compositions had a tail toward the higher wavelength [235]. A similar observation has been made earlier where the presence of tails in absorption spectra was attributed to the surface and intra-band states [180,

190]. The bandgap was estimated by extrapolating the linear region of the Tauc plot [224, 236, 237]. The band edge of wz-CIS and wz-CGS NPs was around 1.49 eV (λ ≈ 833 nm) and 2.0 eV (λ ≈ 652 nm), which was in agreement with the earlier reports [179, 224, 234, 238–240]. Higher absorption in the entire visible and near-infrared region was observed in the case of wz-$CuIn_{0.7}Ga_{0.3}S_2$ NPs **(Figure V.13(b))** when compared to wz-CIS **(Figure V.13(a))** and wz-CGS **(Figure V.13(c))**. A bandgap of ~1.75 eV of $CuIn_{0.7}Ga_{0.3}S_2$ was estimated from the Tauc plot, shown in the inset of **Figure V.13(b)**, which is close to the earlier reported value of 1.78 eV [234]. It was expected that CIGS should exhibit two band edges due to the phase separation (In-rich and In–Ga); however, here we observed only one band edge. This could be because of the fact that the In–Ga phase was present in a significant fraction (0.43), which might have a greater bandgap.

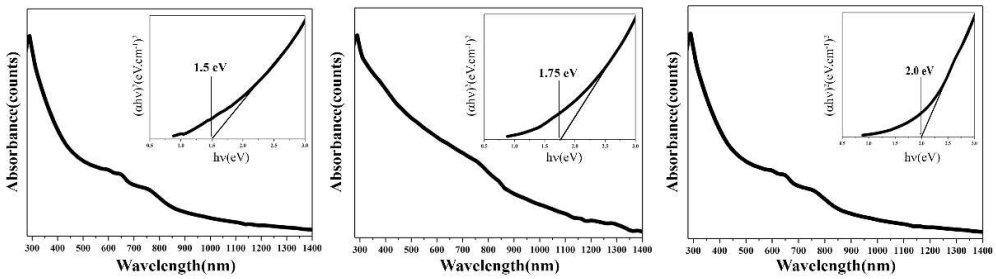

Figure V.13 UV–VIS absorption spectra and Tauc plots (in the insert) of wurtzite nanoparticle of CIS (a), $CuIn_{0.7}Ga_{0.3}S_2$ (b), CGS (c) of the as-synthesized.

V.5 Concluding Remarks

Nanocrystalline wurtzite nanoparticles $CuIn_xGa_{1-x}S_2$ (with x = 1, 0.7, 0.5, 0.3, and 0) were synthesized using the solution processing route. The synthesis was performed using acetylacetonate of copper (II), indium (III), and gallium (III) as

metal precursors, trioctylphosphine as a capping agent, and oleylamine as a solvent and reducing agent. Structural analyses from X-ray diffraction and transmission electron microscopy indicated that the as-synthesized $CuInS_2$ (CIS) and $CuGaS_2$ (CGS) nanoparticles were having single-phase wurtzite structures. On the other hand, $CuIn_xGa_{1-x}S_2$ (CIGS) had more than one wurtzite phases having different morphologies and compositions. The $CuIn_{0.7}Ga_{0.3}S_2$ had two phases with In-rich and In–Ga (1:1) compositions having rod-like and irregular hexagonal morphologies, respectively. On the other hand, on increasing Ga substitution, a third Ga-rich phase (with tadpole morphology) appeared and progressively increased abundance with increasing Ga substitution, while, at the same time, the In-rich phase reduced progressively. The bandgap of the CIGS increased with Ga substitution from 1.49 eV for CIS to 2.0 eV for CGS.